Observation of a Chern insulator in crystalline ABCA-tetralayer graphene with spin-orbit coupling

Yating Sha[1]†, Jian Zheng[1]†, Kai Liu[1]†, Hong Du[2], Kenji Watanabe[3], Takashi Taniguchi[4], Jinfeng Jia[1,2], Zhiwen Shi[1], Ruidan Zhong[2], Guorui Chen[1]*

Degeneracies in multilayer graphene, including spin, valley, and layer degrees of freedom, can be lifted by Coulomb interactions, resulting in rich broken-symmetry states. Here, we report a ferromagnetic state in charge-neutral ABCA-tetralayer graphene driven by proximity-induced spin-orbit coupling from adjacent tungsten diselenide. The ferromagnetic state is identified as a Chern insulator with a Chern number of 4; its maximum Hall resistance reaches 78% quantization at zero magnetic field and is fully quantized at either 0.4 or −1.5 tesla. Three distinct broken-symmetry insulating states, layer-antiferromagnet, Chern insulator, and layer-polarized insulator, along with their transitions, can be continuously tuned by the vertical displacement field. In this system, the magnetic order of the Chern insulator can be switched by three knobs, including magnetic field, electrical doping, and vertical displacement field.

Rhombohedral-stacked multilayer graphene exhibits highly flat conduction and valence bands in the vicinity of the charge-neutral point (CNP), where low-energy bands can be approximately described by a two-band model with an energy-momentum dispersion relation of $E \sim k^N$ (where E represents energy, k represents momentum, and N is the number of layers) (*1*–*5*). As a result, graphene multilayers are anticipated to have strong Coulomb interactions (*6*–*9*). Additionally, the low-energy bands in graphene are largely associated with momentum-space Berry curvatures (*10*) and exhibit multiple degeneracies, including spin, valley, and layer degrees of freedom. These degeneracies are believed to be susceptible to symmetry-breaking effects induced by interactions (*11*–*15*). Therefore, it is predicted that rhombohedral-stacked multilayer graphene can host a diverse range of interaction-driven broken-symmetry states, including the anticipated Chern insulator phase when the top and bottom layers have opposite valley flavors (*12*–*15*). Recent success in fabricating high-quality rhombohedral-stacked multilayer graphene on hexagonal boron nitride (hBN) devices provides promising opportunities to investigate the broken-symmetry states (*16*–*20*).

When the layer number of graphene increases to four, the Coulomb interactions become sufficiently strong to spontaneously break symmetries, leading to layer-resolved charge distribution (layer pseudospin polarization) associated with four spin-valley flavors, in charge-neutral ABCA-tetralayer graphene (ABCA-4LG) on hBN. Recent experiments reported a layer-antiferromagnetic (LAF) insulator, in which the flavors ($K\uparrow$) and ($K'\uparrow$) are polarized in the top layer, with ($K\downarrow$) and ($K'\downarrow$) in the bottom layer (where K and K' correspond to two valleys, $\uparrow$ and $\downarrow$ correspond to two spins), in crystalline ABCA-4LG and ABCAB-pentalayer graphene (*19*–*21*). Such an LAF insulating state is absent in the ABC-trilayer on hBN (*18*, *22*). By applying a large vertical displacement field D, one can manipulate the charge distribution of the flavors. Thus, one expects the emergence of partial and full layer-charge polarizations, which are associated with quantum anomalous Hall (QAH) and quantum valley Hall (QVH), respectively. Indeed, a continuous phase transition from LAF under balanced layer-charge polarization to layer polarized insulator [LPI, also referred as QVH according to certain theory and experimental results (*11*–*13*)] under full layer-charge polarization was observed when increasing the displacement field (*19*). However, QAH, namely a Chern insulator, under partial layer-charge polarization, was absent in this experiment.

Here, we report ferromagnetism in charge-neutral ABCA-4LG by introducing spin-orbit coupling (SOC) from an adjacent layer of WSe_2. Upon tuning D to the intermediate region between the LAF and LPI states, we observed an anomalous Hall hysteretic loop, exhibiting a large Hall resistance $R_{xy} = 5$ kΩ at zero magnetic field B. The R_{xy} value rapidly quantizes to $h/4e^2 \sim 6.4$ kΩ (where h is Planck's constant and e is the electron's charge) at a very low magnetic field of 0.4 T for positive magnetic field (and −1.5 T for the negative side), following the Streda formula with a Chern number $C = 4$, providing evidence that the ferromagnetic state is a high-order Chern insulator (*23*).

Ferromagnetism in ABCA-tetralayer graphene with WSe_2

The presence of ABCA-4LG domains in exfoliated tetralayer graphene flakes was confirmed using scanning near-field infrared microscopy (fig. S1). To stabilize its stacking during subsequent fabrication processes, the ABCA-4LG domain was isolated from adjacent ABAB domains by cutting using an atomic force microscope. Subsequently, the ABCA-4LG domain was encapsulated between exfoliated hBN thin films, with a monolayer of WSe_2 added between ABCA-4LG and the top hBN layer. The resulting heterostructure was fabricated into a Hall bar geometry, featuring one-dimensional (1D) edge contacts, a metal top gate, and a doped silicon bottom gate. Throughout the fabrication procedures, the stacking order of ABCA-4LG under hBN coverage was monitored using the phonon-polariton assisted near-field optical imaging technique (fig. S2D) (*19*). Figure 1A shows an optical image of the device, and Fig. 1B provides a schematic representation [see sections S1 and S2 of (*24*) for further details on WSe_2 crystal growth and device fabrication]. The top and bottom gates enable individual tuning of the doping n and the vertical displacement field D applied to the ABCA-4LG [see section S3 of (*24*)].

Transport measurements were conducted on ABCA-4LG both with and without WSe_2. In the case of ABCA-4LG without WSe_2, as shown in fig. S3A, two peaks in the longitudinal resistance R_{xx} are observed at CNP for $D = 0$ and large $|D|$. These peaks correspond to the interaction-driven LAF insulator and LPI states, respectively (*18*, *21*). A low-resistance region near $|D| \sim 0.1$ V/nm connects these two insulators, indicating a gap closure during the continuous phase transition from LAF to LPI. The Hall resistance R_{xy} at a magnetic field $|B| = 0.5$ T in fig. S3B exhibits the expected sign change across the CNP for the entire range of D. In ABCA-4LG with WSe_2 (Fig. 1C), R_{xx} displays similar features of LAF and LPI at the CNP for both zero and large $|D|$. However, in the R_{xy} measurement shown in Fig. 1D, at intermediate values of D near ±0.1 V/nm, the sign change of R_{xy} shifts toward the positive n side, resulting in a prominent R_{xy} at the CNP. Considering that the only difference between these two devices is the presence of WSe_2, the distinct nonzero R_{xy} at the CNP can be attributed to WSe_2.

To investigate the large R_{xy} at CNP for intermediate D in ABCA-4LG with WSe_2, we measured its magnetic field dependence. Figure 1E clearly shows the hysteretic anomalous Hall effect, providing clear evidence for the ferromagnetism in ABCA-4LG with WSe_2. As a comparison, when we performed the same

[1]Key Laboratory of Artificial Structures and Quantum Control (Ministry of Education), Shenyang National Laboratory for Materials Science, School of Physics and Astronomy, Shanghai Jiao Tong University, Shanghai 200240, China. [2]Tsung-Dao Lee Institute, Shanghai Jiao Tong University, Shanghai, 201210, China. [3]Research Center for Electronic and Optical Materials, National Institute for Materials Science, Tsukuba 305-0044, Japan. [4]Research Center for Materials Nanoarchitectonics, National Institute for Materials Science, Tsukuba 305-0044, Japan.
*Corresponding author. Email: chenguorui@sjtu.edu.cn
†These authors contributed equally to this work.

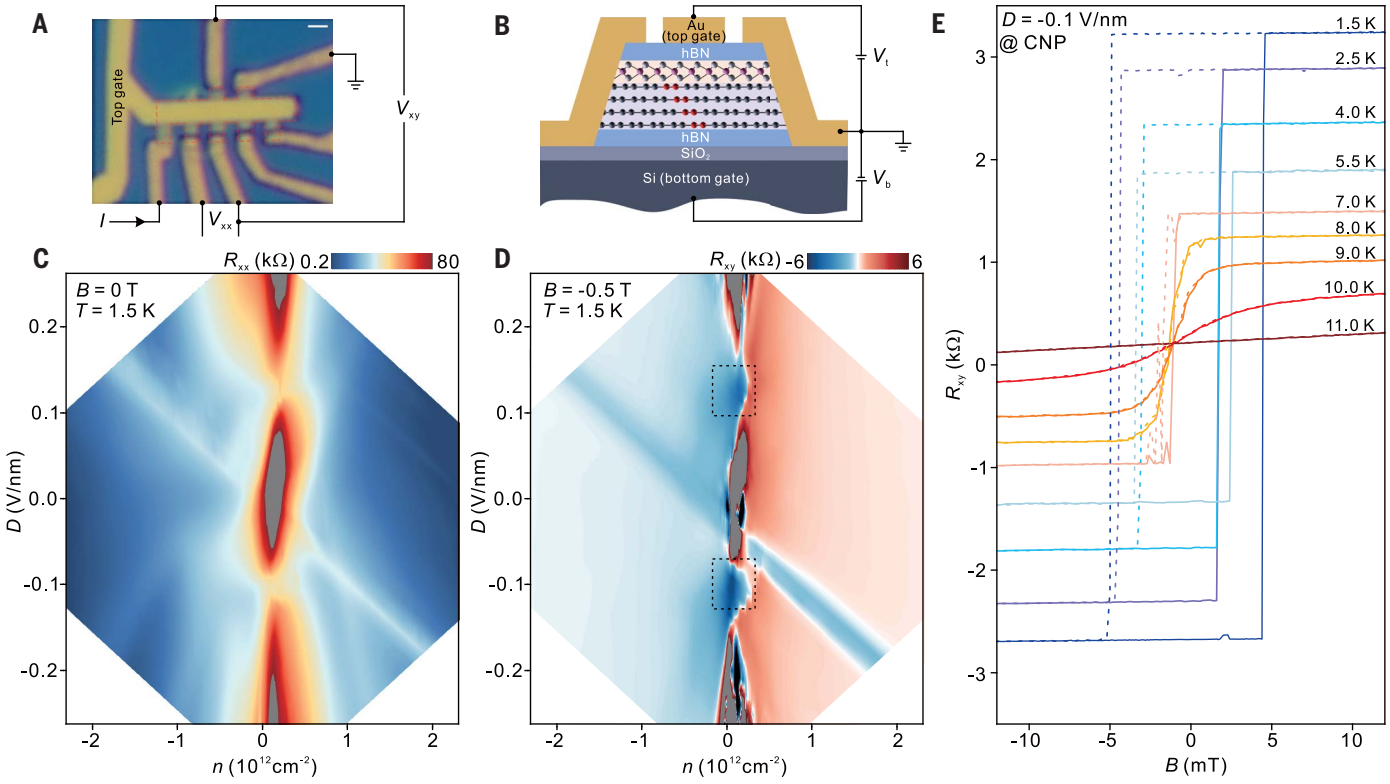

Fig. 1. Schematic and transport of ABCA-4LG with WSe_2. (**A**) Optical image of the hBN/WSe_2/ABCA-4LG/hBN device, including a schematic of the transport measurement configuration. The Hall bar–shaped graphene is highlighted by red dashed line. Scale bar, 1 μm. (**B**) Schematic side view of a dual-gate WSe_2/ABCA-4LG device. The crystal structures of ABCA-4LG and WSe_2 monolayer are shaded by light purple and light orange, respectively. A unit cell of ABCA-4LG is labeled in red. (**C** and **D**) Color plot of longitudinal R_{xx} (C) and Hall R_{xy} (D) resistance at T = 1.5 K as a function of carrier density n and displacement field D. R_{xx} is measured under zero magnetic field, showing insulating states at D = 0 V/nm and large $|D|$. R_{xy} is measured at a low magnetic field, B = −0.5 T. The dashed rectangles near D = ±0.1 V/nm in (D) outline the regions of Chern insulator, where the sign change of R_{xy} shifts toward the positive n side, resulting in a large R_{xy} at the CNP. The gray and black regions represent larger and smaller values than the color scales, respectively. (**E**) Hysteresis loops of anomalous Hall signals at CNP and D = −0.1 V/nm at various temperatures above T = 1.5 K.

measurements on ABCA-4LG without WSe_2, no ferromagnetic behavior was observed under the same conditions (fig. S3D). It is believed that SOC on the order of milli–electron volts can be introduced into graphene through proximity with WSe_2 because of the hybridization between electron wave functions of the two crystals (*25*, *26*). The hysteresis of R_{xy} disappears as the temperature increases to 11 K (Fig. 1E), which is consistent with the calculated and experimental estimates of the proximity-induced SOC strength of ~1 meV in twisted or Bernal bilayer graphene with WSe_2 (*27*–*30*). Although the intrinsic SOC in graphene was theoretically predicted to stabilize a 2D quantum spin Hall topological insulator (*31*), in practice, the intrinsic SOC is negligible (on the order of micro–electron volts) (*32*–*34*). However, the proximity-induced SOC in graphene is significant and has been predicted to give rise to topological phases in multilayer graphene (*26*, *35*).

Topological phases

To explore the topological phase in ABCA-4LG with SOC, we further cooled down the sample to T = 0.1 K and performed measurements of R_{xy} and R_{xx} as a function of n and B at D = −0.1 V/nm. The anomalous Hall signal at D = +0.1 V/nm was less pronounced (fig. S8); a discussion of this $D \leftrightarrow -D$ asymmetry can be found in section S5 of (*24*). The inset of Fig. 2C displays the hysteresis of R_{xy}, highlighting that the R_{xy} value increases to a maximum of 5 kΩ at zero magnetic field and T = 0.1 K. Figure 2B shows that the large R_{xy} signal persists over a range of ~−0.1 to 0.4 × 10^{12} cm^{-2} and exhibits a sharp sign reversal near zero magnetic field due to the anomalous Hall effect. At a very low field of +0.4 T, the R_{xy} is rapidly quantized at 6.4 kΩ, corresponding to a quantum Hall resistance of $h/4e^2$, following the Streda formula $n = \nu eB/h$ for ν = 4, where ν is the filling factor of Landau levels. The presence of the ν = 4 quantum Hall state is further evidenced by the corresponding R_{xx} fan diagram shown in Fig. 2A, where a minimum in R_{xx} starts to develop along the slope of the ν = 4 quantum Hall states, represented by the dashed lines.

The observed quantum Hall state in the presence of a magnetic field is, in fact, a manifestation of the QAH effect in a Chern insulator with a Chern number C = 4. First, when sweeping the magnetic field back and forth within a small range of ±0.2 T at CNP and D = −0.1 V/nm, we clearly observed an anomalous Hall signal exhibiting a ferromagnetic hysteresis loop. The measured anomalous Hall signals of R_{xy} = 5.0 kΩ and 3.5 kΩ for up and down sweeps of the magnetic field, respectively, correspond to 78% and 55% of the quantized R_{xy} value of $h/4e^2$. We emphasize that the data presented in the main text are displayed in their raw form, and have not undergone any processing such as symmetrization or antisymmetrization. The emergence of the anomalous Hall signal signifies the breaking of time-reversal symmetry and the presence of ferromagnetism, both of which are hallmarks of the Chern insulator (*36*–*41*). Second, both the resistance R_{xx} and the conductivity σ_{xx} at zero magnetic field decrease with decreasing temperature (fig. S7), suggesting the quantum Hall type insulating behavior at zero magnetic field. This is indicative of the presence of an exchange gap, which is also consistent with a Chern insulator. At the same time, the temperature dependence of R_{xy} suggests that the incomplete quantization

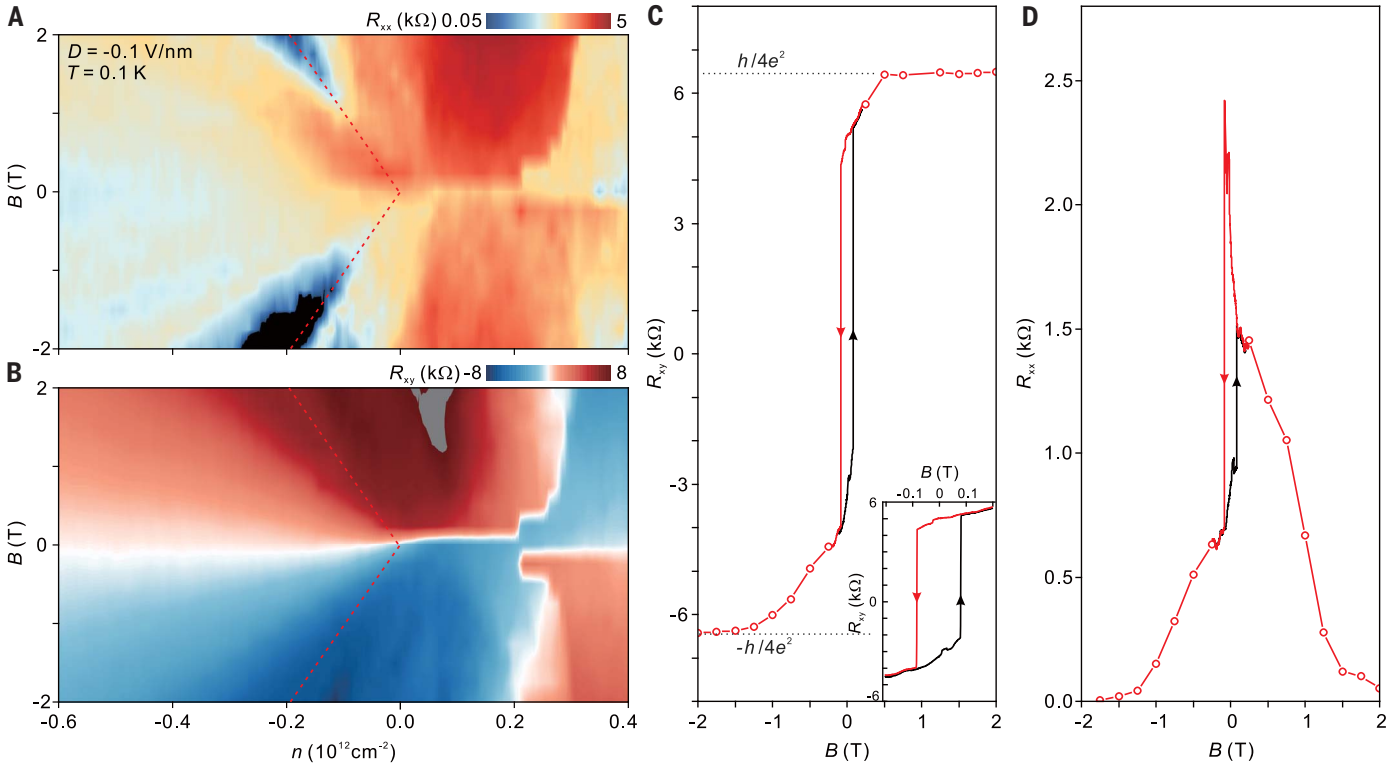

Fig. 2. Chern insulator and magnetic field–stabilized QAH effect at *D* = −0.1 V/nm. (**A** and **B**) Color plot of R_{xx} (A) and R_{xy} (B) as a function of carrier density *n* and magnetic field *B* at *D* = −0.1 V/nm and *T* = 0.1 K. The ν = 4 quantum Hall state can be identified following the Streda formula (denoted by the red dashed lines). Near zero magnetic field, R_{xy} exhibits a sharp sign reversal, indicating the presence of the anomalous Hall effect. Field is swept from positive to negative (namely sweeping down) in both plots. (**C** and **D**) Magnetic field–dependent R_{xx} and R_{xy} at *D* = −0.1 V/nm. Data within a small range of *B* = ±0.2 T are collected from continuous *B* sweeping up and down [see inset of (C) for magnification]. At higher *B* fields, data points (empty circles) of R_{xx} and R_{xy} are acquired along the dashed lines in (A) and (B) following the Streda formula.

of Hall resistance at zero magnetic field may be attributed to sample quality issues, for example, nonuniform proximity-induced SOC (caused by inhomogeneous interface) or defects in the WSe_2 crystal. Third, only ν = 4 quantum Hall state emerges within the range of ±2 T, which is a characteristic feature of a quantized anomalous Hall state. Otherwise, additional quantum Hall states would be expected to develop (*8*, *19*, *20*). Indeed, when tuning *D* outside the range of the anomalous Hall region, a series of quantum Hall states emerge, as shown in fig. S9. Finally, the Hall angle at zero magnetic field, defined as ρ_{xy}/ρ_{xx}, exhibits a large value of 3.6 [which is at least two orders of magnitude larger than the expected values for extrinsic mechanisms in most ferromagnetic materials (*42*)], indicating an intrinsic mechanism for the anomalous Hall and, consequently, the nontrivial band topology.

Following upon the discussions on the Chern insulator, we present the magnetic field-stabilized QAH effect in Fig. 2, C and D. The longitudinal and Hall resistances are plotted as a function of the magnetic field along the dashed lines in Fig. 2, A and B, respectively, in accordance with the Streda formula for a Chern number *C* = ±4. The sign of the Chern number is reflected in the sign of R_{xy} and can be switched by controlling the magnetic field. The ferromagnetic hysteretic behavior for other values of *n* and *D* are shown in fig. S10.

Breaking symmetry

Next, by examining the broken-symmetry states and their transitions along tuning the displacement field for charge-neutral ABCA-4LG with and without WSe_2, we were able to gain valuable insights into the emergence of the Chern insulator. In the case of ABCA-4LG without WSe_2, as shown in Fig. 3A and fig. S3, two broken-symmetry correlated insulating states, LAF and LPI, are observed at CNP. LAF emerges at *D* = 0, where two spin-valley flavors, (*K*↑) and (*K*′↑), are polarized in the top layer, whereas the other two flavors, (*K*↓) and (*K*′↓), are polarized in the bottom layer. At large values of *D*, all four spin-valley flavors become polarized in the same layer, resulting in the LPI state. Each spin-valley flavor pair corresponds to a band with a Chern number of ±*N*/2, where *N* (=4 for the tetralayer) represents the number of graphene layers (*13*). The sign of the Chern number depends on both the valley label and the mass term (the sense of layer polarization) in the two-band model of ABCA-4LG (*10*, *13*). For simplicity, the sign can be conveniently represented by the valley-layer locking: a positive sign when *K*(*K*′) is polarized in the top (bottom) layer and a negative sign when *K*(*K*′) is polarized in the bottom (top) layer. Following this criterion, for LAF, depicted as the gray diagram in Fig. 3C, the Chern number of (*K*↑), (*K*′↑), (*K*↓), and (*K*′↓) are 2, −2, −2, and 2, respectively, resulting in a zero total Chern number and indicating a topological trivial state. Similarly, for LPI, illustrated as the blue diagram in Fig. 3C, (*K*↓) and (*K*′↓) are transferred from the bottom layer to the top layer, with the signs of their Chern numbers reversing and becoming 2 and −2, respectively. As a result, the total Chern number remains zero for LPI (fig. S6). In the intermediate region between LAF and LPI, R_{xx} continuously decreases to as low as ~2 kΩ and exhibits metallic temperature dependence at low temperatures (fig. S3C). Additionally, no anomalous Hall effect is observed (fig. S3, B and D), indicating a gap closure at *D* ~ 0.1 V/nm. These broken-symmetry insulating states in ABCA-4LG without WSe_2 are driven by strong Coulomb interactions in the intrinsic flat bands of ABCA-4LG, which allows the breaking of

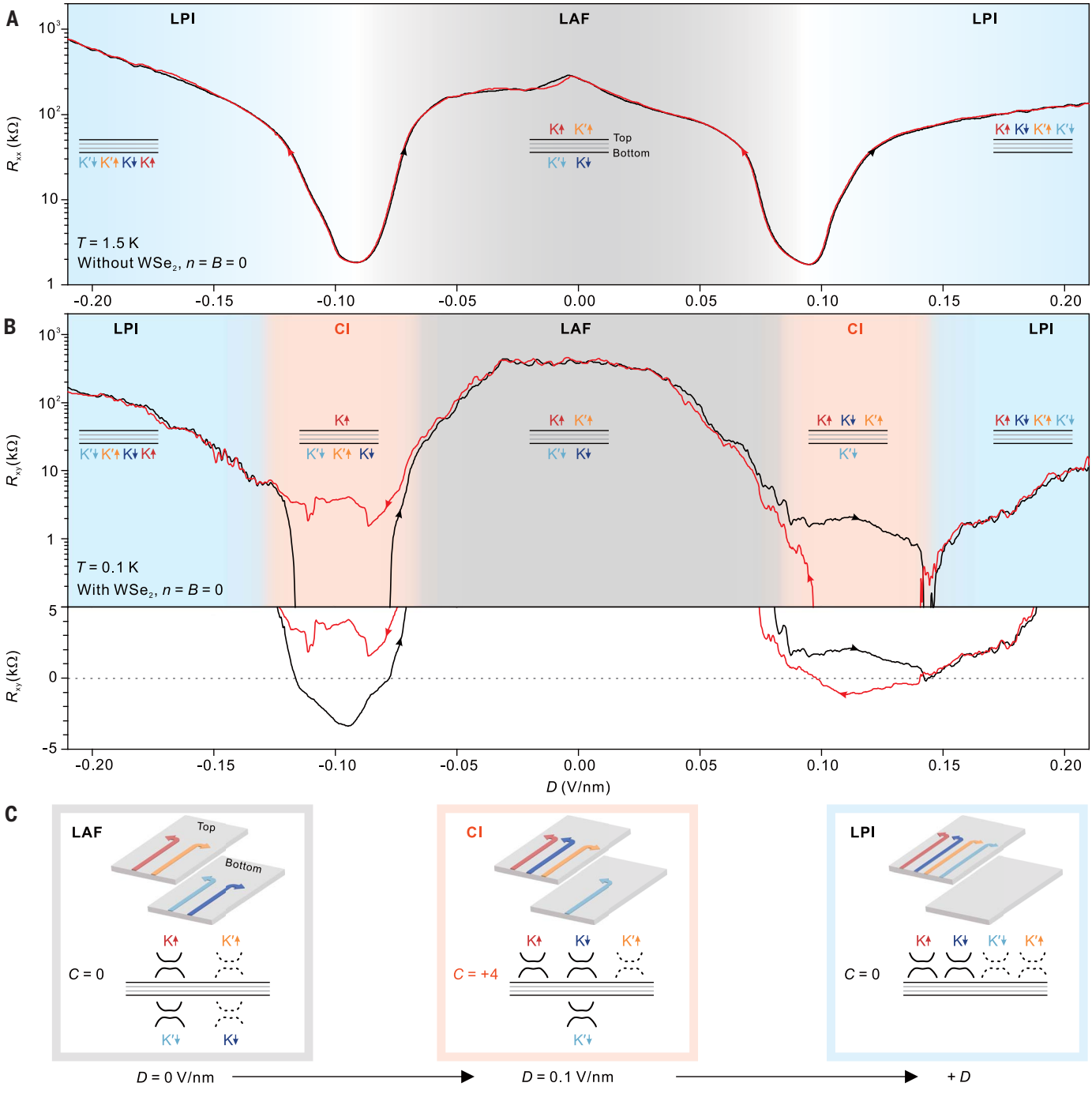

Fig. 3. Broken-symmetry states at CNP in ABCA-4LG with and without SOC. (**A**) R_{xx} as a function of D at B = 0 T in ABCA-4LG without SOC (WSe_2). Gray and blue shaded regions correspond to the interaction-driven LAF and LPI states, respectively. (**B**) R_{xy} as a function of D at B = 0 T in ABCA-4LG with SOC (WSe_2). In addition to LAF and LPI states, the CI states are observed with hysteresis loops at D = ±0.1 V/nm (orange shaded regions in the top panel). The bottom panel shows a magnified plot of R_{xy} in linear scale. Inset schematics in (A) and (B) indicate the layer polarization of spin-valley flavors for different broken-symmetry states (for the CI state, only one representative polarization phase is presented; the complete phase diagram is shown in fig. S13). The black and gray lines in the inset represent four graphene layers. Valleys and spins are represented by K, K', and ↓, ↑. (**C**) Schematics of the Chern numbers and Hall conductivity contributions of four spin-valley flavor pairs for different broken-symmetry states. Each spin-valley flavor pair corresponds to a band with a Chern number of ±2, denoted by solid (+2) or dashed (−2) bands in the bottom panels, respectively. The directions (left and right) of the arrows in the top panels represent the corresponding Hall conductivity contributions ($+2e^2/h$ and $-2e^2/h$). Only holes in the occupied valence band are considered here. A more comprehensive diagram is shown in figs. S5 and S6 for ABCA-4LG with and without WSe_2, respectively.

time-reversal symmetry (T) and inversion symmetry (I) while preserving the valley-Ising symmetry ($\mathcal{Z}_2$) (*13*, *43*), leading to the absence of Chern insulator.

By comparison, Fig. 3B shows R_{xy} as a function of D at CNP for ABCA-4LG with WSe_2 (fig. S4 shows a direct comparison of R_{xy}-D data in ABCA-4LG with and without WSe_2). As D is swept, the LAF and LPI states are not evidently affected by SOC because of their large energy gaps (*19*, *21*). However, SOC plays a crucial role in the intermediate state between LAF and LPI, leading to the emergence of a Chern insulator state. The Chern insulator can be attributed to a band inversion of one flavor pair, driven by the proximity-induced SOC. At intermediate D = 0.1 V/nm, shown as the orange diagram in Fig. 3C, ($K\downarrow$) is transferred from the bottom layer to the top layer, resulting in a sign change of its Chern number from −2 to 2. This sign change leads to a total Chern number of 4 (= 2 + 2 + 2 − 2) when adding up the Chern numbers of all four flavor pairs. In addition to breaking the time-reversal symmetry and inversion symmetry, the interplay of SOC and strong Coulomb interactions can further break the $\mathcal{Z}_2$ symmetry, driving the formation of the Chern insulator state. We provide a diagram for the detailed mechanism by which SOC stabilizes the Chern insulator state in fig. S5.

Controlling the magnetic order

The observed Chern number C = ±4 in ABCA-4LG with WSe_2 is compatible with the predicted flavor ferrimagnetic (Fi) state for partial layer-charge polarization in rhombohedral multilayer graphene. Such states have associated "ALL" quantum Hall phases, including quantum anomalous charge, spin, valley, and spin-valley Hall state (hence the name) (fig. S13) (*13*, *44*). Our transport measurements primarily detected the quantum anomalous charge Hall effect in ABCA-4LG with SOC, indicating a promising system for further exploration of quantum anomalous spin, valley, and spin-valley Hall effects using spin- and valley-sensitive probes. There are four possible layer-flavor polarization configurations for the "ALL" state at a given D (as shown in fig. S13), which correspond to different magnetic states, or namely the Chern numbers. Therefore, one can expect to manipulate the magnetic order in this 3D parameter space (B, n, D).

The magnetic order, represented by the sign of the anomalous Hall resistance ($\Delta R^B_{xy} = R^{B\uparrow}_{xy} - R^{B\downarrow}_{xy}$), exhibits dependence on n. In Fig. 4A, a sign reversal of ΔR^B_{xy} is observed when n slightly crosses CNP at ~0.28×10^{12} cm^{-2}, indicating a switching of the magnetic order as the Fermi level crosses the band gap. Figure 4B presents representative line cuts from Fig. 4A at different n values. The magnetic order can be directly switched by tuning n at fixed B. At fixed magnetic fields ranging from 0.28 T to −0.26 T, hysteresis loops of R_{xy} in the n-axis are observed, indicating the switching of the magnetic order as n is swept back and forth (Fig. 4D). The sign reversal of $\Delta R^n_{xy} = R^{n\uparrow}_{xy} - R^{n\downarrow}_{xy}$ occurs when the magnetic field crosses zero (Fig. 4C). This demonstrates that the magnetic order of the Chern insulator at CNP can be individually controlled by B and n, as shown in Fig. 4E. Similar electrically tunable magnetism in Chern insulators has been reported in twisted graphene systems (*45*–*47*), where the net magnetization has two contributions, one from the bulk stemming from a certain valley polarization and the other from the edge state, which can reverse sign when tuning the doping inside the topological gap (*48*). However,

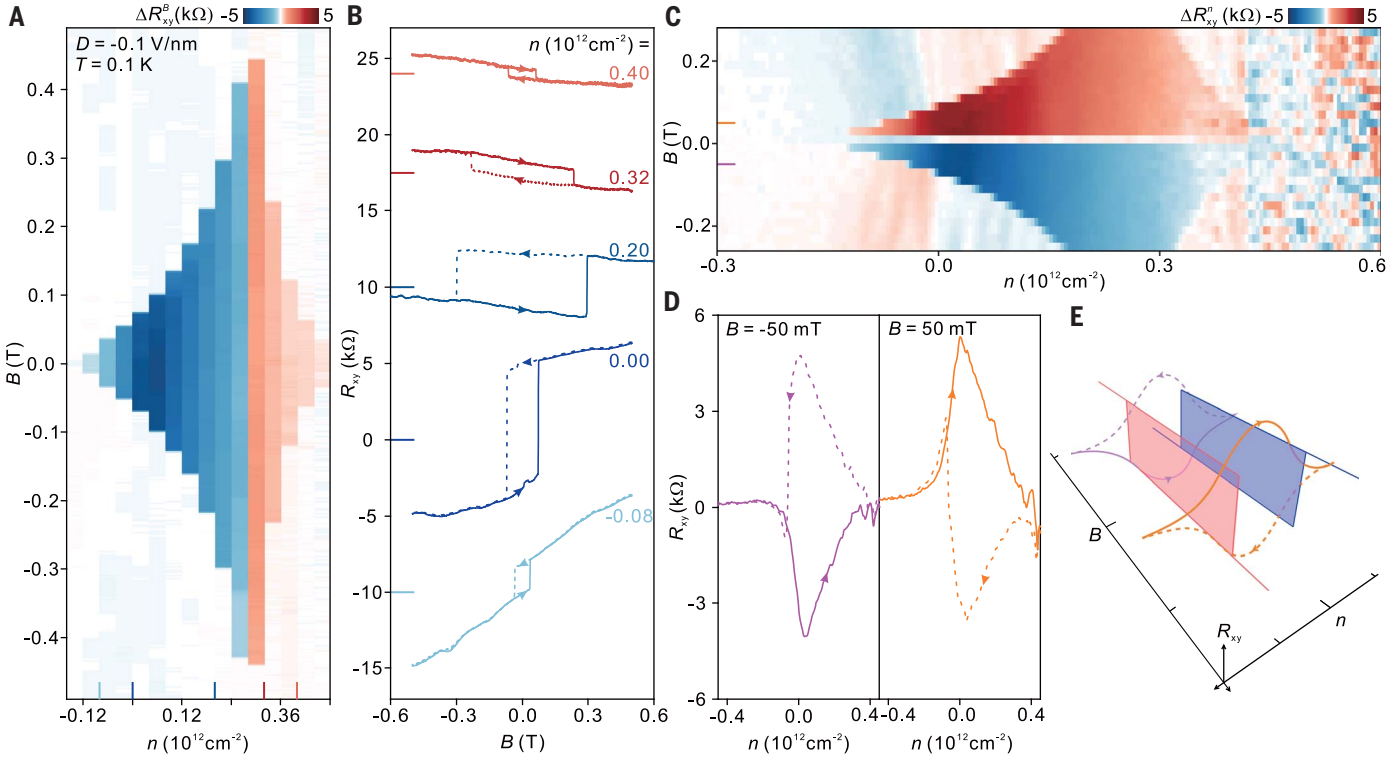

Fig. 4. Electrical switching of the magnetic order. (**A**) Anomalous Hall resistance when sweeping B, defined by $\Delta R^B_{xy} = R^{B\uparrow}_{xy} - R^{B\downarrow}_{xy}$ and represented by colors, at different dopings near CNP at D = −0.1 V/nm and T = 0.1 K. An abrupt sign change of ΔR^B_{xy} occurs at ~$n = 0.28 \times 10^{12}$ cm^{-2}. (**B**) Magnetic hysteresis loops of R_{xy} at $n = 0.4 \times 10^{12}$, 0.32×10^{12}, 0.2×10^{12}, 0, and -0.08×10^{12} cm^{-2}, with colors corresponding to the doping positions labeled in (A). Data are vertically offset for clarity. Solid lines on the y axis mark the positions of zero R_{xy} for each curve. (**C**) The anomalous Hall resistance when sweeping n, defined by $\Delta R^n_{xy} = R^{n\uparrow}_{xy} - R^{n\downarrow}_{xy}$, at fixed B ranging from −0.26 T to 0.28 T. Temperature and D are the same as in (A). (**D**) Electrical hysteresis loops of R_{xy} at B = ±50 mT, with colors corresponding to the magnetic fields labeled in (C). (**E**) Schematic of two individual knobs, B and n, of tuning the magnetic order of the Chern insulator at CNP in ABCA-4LG.

in charge-neutral ABCA-4LG with WSe_2, the magnetic order originates from both K and K' valleys, which distinguishes it from the magnetism reported in Moiré systems (fig. S12). The detailed mechanism of the electrically tunable magnetism in such crystalline graphene requires further theoretical investigation.

The magnetic order also exhibits an interesting dependence on the displacement field. Figure 3B (bottom panel) shows hysteresis loops of R_{xy} in D at the Chern insulator states for D = ±0.1 V/nm. When sweeping D from negative to positive, R_{xy} is negative near D = −0.1 V/nm and positive near D = 0.1 V/nm. Conversely, when sweeping D from positive to negative, R_{xy} becomes negative near D = 0.1 V/nm and positive near D = −0.1 V/nm. However, at a magnetic field of B = 10 mT (-10 mT), unlike the sign reversal observed during doping switching, R_{xy} remains positive (negative) for both sweeping directions on both sides of D (fig. S11). The ferromagnetism, and therefore the Chern number in ABCA-4LG/WSe_2, can be switched by three knobs, B, n, and D, represented by a 3D parameter space shown in fig. S13.

Discussion and outlook

We now discuss the specific properties of the Chern insulator state observed in ABCA-4LG with WSe_2. First, its mechanism markedly differs from the Chern insulator states found in doped and/or intrinsic magnetic topological insulators and 2D Moiré superlattices. The time-reversal symmetry breaking emerges from the strong Coulomb interactions within the intrinsic flat band of crystalline graphene, and the nontrivial topology arises from the proximity-induced SOC from WSe_2. Second, the magnetism (and the Chern number) in our system originates from both K and K' valleys in different layers rather than from a single valley as in the Moiré system (fig. S12). Two opposite valleys in different layers contribute to the total Chern number, which is similar to the Haldane model (*36*), in which a valley-contrasting mass term leads to opposite valleys having the same sign of the Berry curvature, leading to a nonzero total Chern number in crystalline graphene. Third, the Chern insulator in ABCA-4LG/WSe_2 is at the charge-neutral point, which differs from the Chern insulators at certain fillings of Moiré superlattices. As a result, the realization of a Chern insulator does not require precise control of the twist angle. Finally, the Chern number of 4 precisely matches the winding number of ABCA-4LG, which implies an approach to developing a Chern insulator family with controllable Chern numbers by varying the layer number in thicker rhombohedral multilayer graphene with SOC.

Our experiment showcases a system to achieve a Chern insulator state based on a tunable LAF with SOC. Featuring highly tunable symmetries within one sample, including charge, spin, valley, layer, and SOC, ABCA-4LG/WSe_2 offers a flexible and versatile platform for further study. This simple structure also opens up avenues for investigating topological phase transitions and potentially exploring topological phases such as topological superconductors and fractional Chern insulators. Additionally, the layer-dependent Chern numbers in rhombohedral multilayer graphene establish this system as a valuable natural crystal resource of high-order Chern insulators for multichannel quantum computing.

REFERENCES AND NOTES

1. M. Koshino, E. McCann, *Phys. Rev. B* **80**, 165409 (2009).
2. F. Zhang, B. Sahu, H. Min, A. H. MacDonald, *Phys. Rev. B* **82**, 035409 (2010).
3. H. Min, A. H. MacDonald, *Prog. Theor. Phys. Suppl.* **176**, 227–252 (2008).
4. M. Koshino, *Phys. Rev. B* **81**, 125304 (2010).
5. M. Aoki, H. Amawashi, *Solid State Commun.* **142**, 123–127 (2007).
6. W. Bao *et al*., *Nat. Phys.* **7**, 948–952 (2011).
7. A. Kerelsky *et al*., *Proc. Natl. Acad. Sci. U.S.A.* **118**, e2017366118 (2021).
8. Y. Shi *et al*., *Nature* **584**, 210–214 (2020).
9. Z. Lu *et al*., *Nature* **626**, 759–764 (2024).
10. D. Xiao, M.-C. Chang, Q. Niu, *Rev. Mod. Phys.* **82**, 1959–2007 (2010).
11. J. Velasco Jr. *et al*., *Nat. Nanotechnol.* **7**, 156–160 (2012).
12. Y. Lee *et al*., *Nat. Commun.* **5**, 5656 (2014).
13. F. Zhang, J. Jung, G. A. Fiete, Q. Niu, A. H. MacDonald, *Phys. Rev. Lett.* **106**, 156801 (2011).
14. J. Jung, A. H. MacDonald, *Phys. Rev. B* **88**, 075408 (2013).
15. F. Zhang, *Synth. Met.* **210**, 9–18 (2015).
16. G. Chen *et al*., *Nature* **579**, 56–61 (2020).
17. G. Chen *et al*., *Nano Lett.* **22**, 238–245 (2022).
18. H. Zhou *et al*., *Nature* **598**, 429–433 (2021).
19. K. Liu *et al*., *Nat. Nanotechnol.* **19**, 188–195 (2024).
20. T. Han *et al*., *Nat. Nanotechnol.* **19**, 181–187 (2024).
21. K. Myhro *et al*., *2D Mater.* **5**, 045013 (2018).
22. G. Chen *et al*., *Nat. Phys.* **15**, 237–241 (2019).
23. Y.-F. Zhao *et al*., *Nature* **588**, 419–423 (2020).
24. See the supplementary materials for methods and detailed analysis.
25. Y. Li, M. Koshino, *Phys. Rev. B* **99**, 075438 (2019).
26. M. Gmitra, D. Kochan, P. Högl, J. Fabian, *Phys. Rev. B* **93**, 155104 (2016).
27. J.-X. Lin *et al*., *Science* **375**, 437–441 (2022).
28. J. O. Island *et al*., *Nature* **571**, 85–89 (2019).
29. Y. Zhang *et al*., *Nature* **613**, 268–273 (2023).
30. D. Wang *et al*., *Nano Lett.* **19**, 7028–7034 (2019).
31. C. L. Kane, E. J. Mele, *Phys. Rev. Lett.* **95**, 226801 (2005).
32. H. Min *et al*., *Phys. Rev. B* **74**, 165310 (2006).
33. Y. Yao, F. Ye, X.-L. Qi, S.-C. Zhang, Z. Fang, *Phys. Rev. B* **75**, 041401 (2007).
34. S. Konschuh, M. Gmitra, D. Kochan, J. Fabian, *Phys. Rev. B* **85**, 115423 (2012).
35. Z. Qiao *et al*., *Phys. Rev. B* **82**, 161414 (2010).
36. F. D. M. Haldane, *Phys. Rev. Lett.* **61**, 2015–2018 (1988).
37. C.-Z. Chang *et al*., *Science* **340**, 167–170 (2013).
38. Y. Deng *et al*., *Science* **367**, 895–900 (2020).
39. T. Li *et al*., *Nature* **600**, 641–646 (2021).
40. A. L. Sharpe *et al*., *Nano Lett.* **21**, 4299–4304 (2021).
41. C.-C. Tseng *et al*., *Nat. Phys.* **18**, 1038–1042 (2022).
42. N. Nagaosa, J. Sinova, S. Onoda, A. H. MacDonald, N. P. Ong, *Rev. Mod. Phys.* **82**, 1539–1592 (2010).
43. F. Zhang, A. H. MacDonald, *Phys. Rev. Lett.* **108**, 186804 (2012).
44. F. R. Geisenhof *et al*., *Nature* **598**, 53–58 (2021).
45. S. Chen *et al*., *Nat. Phys.* **17**, 374–380 (2021).
46. H. Polshyn *et al*., *Nature* **588**, 66–70 (2020).
47. C. L. Tschirhart *et al*., *Science* **372**, 1323–1327 (2021).
48. J. Zhu, J.-J. Su, A. H. MacDonald, *Phys. Rev. Lett.* **125**, 227702 (2020).
49. Y. Sha *et al*., Data for: Observation of Chern insulator in crystalline ABCA-tetralayer graphene with spin-orbit coupling, Dryad (2024); https://doi.org/10.5061/dryad.dncjsxm6d.

ACKNOWLEDGMENTS

We thank F. Wu, Z. Qiao, J. Jung, W. Luo, and Y. Zhang for helpful discussions. **Funding:** G.C. acknowledges support from National Key Research Program of China (grant nos. 2021YFA1400100 and 2020YFA0309000), NSF of China (grant nos. 12350005 and 12174248), SJTU (grant no. 21X010200846) and the Yangyang Development Fund. R.Z. acknowledges support from the Ministry of Science and Technology of China (grant nos. 2022YFA1402702 and 2021YFA1401600) and NSF of China (grant nos. 12334008 and 12374148). Z.S. acknowledges support from the National Key Research Program of China (grant no. 2021YFA1202902) and NSF of China (grant nos. 12074244 and 12374292). J.J. acknowledges support from the Ministry of Science and Technology of China (grant no. 2019YFA0308600). K.W. and T.T. acknowledge support from the Japan Society for the Promotion of Science (JSPS) (KAKENHI grant nos. 20H00354, 21H05233, and 23H02052) and the World Premier International Research Center Initiative (WPI), MEXT, Japan. **Author contributions:** G.C. conceived and supervised the project. Y.S. and K.L. fabricated the devices with and without WSe_2, respectively. Y.S., J.Z., and K.L. performed the transport measurements. J.Z. set up the dilution refrigerator. H.D. and R.Z. grew the WSe_2 bulk crystals. K.W. and T.T. grew the hBN bulk crystals. Y.S., J.Z., K.L., and G.C. analyzed the data. Y.S. and G.C. wrote the paper with input from all authors. **Competing interests:** The authors declare no competing interests. **Data and materials availability:** The data from this study are available at Dryad (*49*).